

# Compressive mechanical properties and shape memory effect of NiTi gradient lattice structures fabricated by laser powder bed fusion

Wei Chen<sup>1</sup>, Dongdong Gu<sup>1,\*</sup>, Jiankai Yang<sup>1</sup>, Qin Yang<sup>2</sup>, Jie Chen<sup>2</sup> and Xianfeng Shen<sup>2</sup>

<sup>1</sup> Jiangsu Provincial Engineering Laboratory for Laser Additive Manufacturing of High-Performance Metallic Components, College of Materials Science and Technology, Nanjing University of Aeronautics and Astronautics, Yudao Street 29, Nanjing 210016, People's Republic of China

<sup>2</sup> Institute of Machinery Manufacturing Technology, China Academy of Engineering Physics, Mianyang, Sichuan 621000, People's Republic of China

E-mail: [dongdonggu@nuaa.edu.cn](mailto:dongdonggu@nuaa.edu.cn)

Received 20 December 2021, revised 6 March 2022

Accepted for publication 1 September 2022

Published 5 October 2022



## Abstract

Laser additive manufacturing (AM) of lattice structures with light weight, excellent impact resistance, and energy absorption performance is receiving considerable attention in aerospace, transportation, and mechanical equipment application fields. In this study, we designed four gradient lattice structures (GLSs) using the topology optimization method, including the unidirectional GLS, the bi-directional increasing GLS, the bi-directional decreasing GLS and the none-GLS. All GLSs were manufactured by laser powder bed fusion (LPBF). The uniaxial compression tests and finite element analysis were conducted to investigate the influence of gradient distribution features on deformation modes and energy absorption performance of GLSs. The results showed that, compared with the 45° shear fracture characteristic of the none-GLS, the unidirectional GLS, the bi-directional increasing GLS and the bi-directional decreasing GLS had the characteristics of the layer-by-layer fracture, showing considerably improved energy absorption capacity. The bi-directional increasing GLS showed a unique combination of shear fracture and layer-by-layer fracture, having the optimal energy absorption performance with energy absorption and specific energy absorption of 235.6 J and 9.5 J g<sup>-1</sup> at 0.5 strain, respectively. Combined with the shape memory effect of NiTi alloy, multiple compression-heat recovery experiments were carried out to verify the shape memory function of LPBF-processed NiTi GLSs. These findings have potential value for the future design of GLSs and the realization of shape memory function of NiTi components through laser AM.

Keywords: additive manufacturing, laser powder bed fusion, gradient lattice structures, deformation behavior, shape memory effect

\* Author to whom any correspondence should be addressed.



Original content from this work may be used under the terms of the [Creative Commons Attribution 4.0 licence](#). Any further distribution of this work must maintain attribution to the author(s) and the title of the work, journal citation and DOI.

## 1. Introduction

Lattice structures are generally defined as porous structures obtained by the repeated arrangement of unit cells in space [1]. As a favorable functional material, lattice structure has remarkable mechanical properties and unique advantages, such as lightweight [2], high specific strength and rigidity [3], excellent energy absorption capacity [4], heat dissipation [5], electromagnetic shielding [6], and biocompatibility [7]. Therefore, lattice structures have been widely used in aerospace industries [8], biomedical science [9] and transportation engineering [10]. As the basic elements in lattice structures, unit cells greatly determine the performance and functional properties of the overall structures. Tamburrino *et al* classified the 3D unit cell structures into three categories [11]: (a) triply periodic minimal surfaces [12, 13]; (b) truss and node arrangement (truss) [14–18]; (c) 3D custom structures, such as bionic unit cells [19–21].

The innovative designs of unit cell configurations promote the research and development of lattice structures. The design methods of unit cells mainly include the primitive-based method [22], the implicit surface-based method [23], and the topology optimization (TO) method [24]. The primitive-based method is a straightforward approach relying on the combination of basic geometric elements [25]. The implicit surface-based method uses mathematical formulations to quantitatively describe the geometric characteristics of the unit cell [26]. However, these two methods still have some limitations such as limited software packages for structural design optimization and unpredictable mechanical properties [27]. TO is a mathematical method capable of optimizing structural material distribution and maximizing performance based on boundary constraints and loading conditions [28, 29]. TO can reasonably distribute materials according to the optimal force transmission path to optimize the structure, which has a high degree of designability and can realize the design of lattice structures [30, 31]. The unit cells with different relative densities can be obtained based on the TO method. For example, Xiao *et al* [32] designed three different lattice structures with high strength and rigidity by changing the load position in the TO process. Zhang *et al* [33] used the TO method and laser powder bed fusion (LPBF) to design and manufacture the lightweight and high-performance lattice structure, which can achieve a high energy absorption efficiency of 67.9% at a strain of 0.15. TO has become a widely used method for designing lattice structures.

Gradient lattice structures (GLSs) can realize different deformation modes and mechanical properties by varying the spatial relative density distributions [34], having potential applications in aerospace, transportation, and medical devices [35, 36]. Previous design methods to achieve variable density in space [37–39] are mainly changing strut diameter, strut length, wall thickness, or unit cell (changing the size of the unit cell or combining multiple unit cell structures). The combination of gradient design and the TO methods provides the possibility to further improve the mechanical and functional properties of the lattice structures.

The traditional manufacturing methods of porous structures mainly include powder metallurgy, melt foaming, and investment casting [40]. However, they are limited in forming lattice structures with complex unit cells and high forming accuracy. Laser powder bed fusion (LPBF) is a typical additive manufacturing (AM) technology [41, 42], in which powders are rapidly melted and solidified under the action of the laser, enabling the integrated fabrication of components [43]. The high manufacturing precision of LPBF improves the formability of complex lattice structures [44–46].

At present, the materials used in LPBF of metallic lattice structures mainly include stainless steel, Al alloys, and Ti alloys [14, 16, 47]. These traditional elastic-plastic materials usually have the disadvantage of being difficult to reuse after plastic deformation, leading to the inability of these materials to meet the needs of multi-functional and multiple-recycled components. NiTi shape memory alloy is expected to overcome these shortcomings and become a new material for lattice structure. NiTi alloy has the advantages of shape memory effect, superelasticity, and biocompatibility. Due to the forming hysteresis energy dissipation loops during loading and unloading processes, NiTi also exhibits the characteristic of high energy absorption [48, 49]. To satisfy the application requirements of the lattice structures in the energy-absorbing components of aerospace field (such as soft-landing spacecraft), it is necessary to improve the deformation recovery function of the lattice structures. NiTi alloy can be used to manufacture the lattice structures that have the functions of bearing and deformation recovery simultaneously.

In this paper, the TO method based on different weight reduction conditions was applied to obtain the unit cells with different relative densities. By reasonably arranging unit cells in the gradient direction, the design process of GLSs was further simplified to reduce the design complexity and calculation cost. Four kinds of NiTi GLSs were processed by LPBF to study the influence of the gradient distributions of unit cells on mechanical properties and energy absorption capacity. The deformation and fracture mechanism during the compression process were studied by compression experiments and finite element analysis (FEA). The shape memory behavior of NiTi lattice structures was studied by multiple compression-heat recovery experiments.

## 2. Experimental procedure

### 2.1. TO and GLS design

The topological optimization module of ANSYS Workbench software was used in this work to optimize the cubic structure with the side length of 5 mm. The mathematical expression of topological optimization is as follows [50]:

$$\left\{ \begin{array}{l} \min F(x) = c(x) \\ \text{s.t } K(x) u = f \\ V(x)/V_0 \leqslant V_f \\ 0 < x_{\min} \leqslant x_i \leqslant 1, i = 1, \dots, n \end{array} \right. . \quad (1)$$

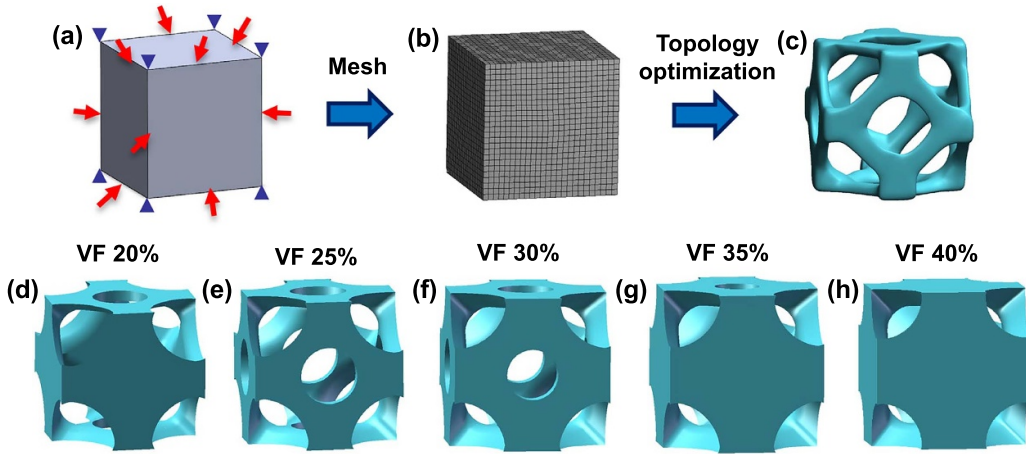


**Figure 1.** Topology optimization processing and model reconstruction of obtained topology structures: (a) load boundary conditions for topology optimization, (b) mesh partitioning model with  $25 \times 25 \times 25$  eight-node brick elements, (c) topology optimized structure based on 70% weight reduction, (d)–(h) reconstructed topology optimization structures with the volume fraction of 20%, 25%, 30%, 35% and 40%, respectively.

$x$  is the design variable of relative density;  $F(x)$  represents the total strain energy function;  $c(x)$  represents the global compliance;  $u$  represents the displacement;  $K(x)$  represents the global stiffness;  $V(x)$  and  $V_0$  are the initial volume of the design area and the volume after TO, respectively; the constraint  $V_f$  is the volume fraction after TO;  $n$  is the number of variables. TO was used as a design method for lightweight load-bearing structures, and the parameters of nonlinear shape memory alloy material were not considered in the TO model.

The base material parameters were referred to the previous report [51].

TO process and results are presented in figure 1. A force of 5000 N in a  $45^\circ$  direction was loaded on the center of each edge of the cube (red arrows in figure 1(a)), and displacement constraints were applied to all eight endpoints (blue triangles in figure 1(a)). The eight-node hexahedral element was adopted to mesh the model (figure 1(b)), where the total number of elements was 15 625. The part where the load was applied was marked as the non-design area. The material in the non-design area will be retained in the TO process to ensure that the optimized structure has a good connection. Total strain energy and volume fraction (VF) were set as responses in the TO process. The total strain energy is the sum of the strain energy of all grid elements, which determines the flexibility of the structure. The VF represents the ratio of the structure volume obtained by the TO method to the original volume, which is used to constrain the number of iteration steps and the final topology configuration. In this study, the volume of the optimized model was constrained to 20%, 25%, 30%, 35%, and 40% of the original volume under the condition of minimum strain energy (figure 1(c) is the optimization result when the VF was 30%). 3D design software SolidWorks was used to reconstruct topology optimized unit cell structures to eliminate irregular edges and corners. As shown in figures 1(d)–(h), the relative densities of the five kinds of unit cells were 0.2, 0.25, 0.3, 0.35, and 0.4, respectively.

Four types of GLSs, namely the unidirectional GLS, the bi-directional increasing GLS, the bi-directional decreasing GLS and the none-GLS were designed by using SolidWorks. The size of the GLSs was  $25 \text{ mm} \times 25 \text{ mm} \times 25 \text{ mm}$ . The CAD models and profiles (gray area) are shown in figure 2, where the red dashed lines are the positions of the profiles. The relative density of the unidirectional GLS varied unidirectionally from 0.40 to 0.20 along the build direction, where the bottom layer had the largest relative density (figure 2(a)). The relative density of the bi-directional increasing GLS increased bidirectionally from 0.20 to 0.35, with the lowest relative density in the middle layer (figure 2(b)). The relative density of the bi-directional decreasing GLS decreased bidirectionally from 0.40 to 0.25, with the highest relative density in the middle layer (figure 2(c)). The none-GLS consisted of unit cells with densities of 0.30 was designed as a comparison (figure 2(d)). The average relative density of the four GLSs was 0.3. In this study, the TO design of the unit cell was considered a minimization of compliance, while the gradient design was aimed at improving the energy absorption capacity of the lattice structure. The combination of TO and gradient design not only facilitated the design of the GLS, but also realized the combination of high bearing capacity and high energy absorption capacity of the lattice structure.

## 2.2. LPBF processing

NiTi pre-alloyed powder with a nominal composition of  $\text{Ni}_{50.6}\text{Ti}_{49.4}$  and particle size distribution of 15–53  $\mu\text{m}$  was selected (figure 3(a)). NiTi lattice structures were processed by the LPBF-150 equipment. The LPBF system (figure 3(b)) mainly consisted of a YLR-500-WC ytterbium fiber laser (IPG Laser GmbH, Germany), a powder spreading device, an inert argon gas protection system, and an automatic processing control system. The maximum power of the laser can reach 500 W, and the spot diameter is 70  $\mu\text{m}$ . Due to

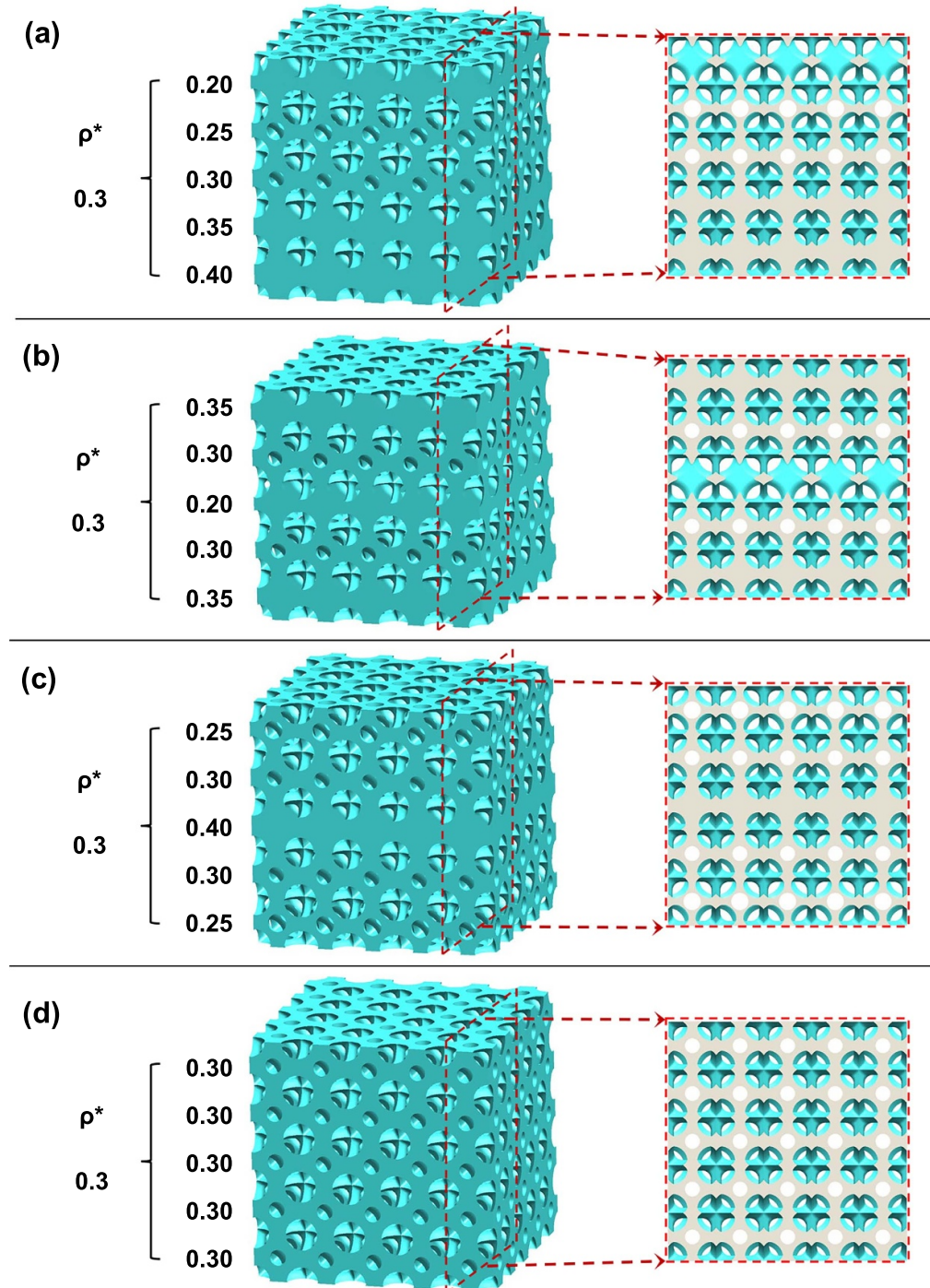


**Figure 2.** CAD models (left) and profiles (right) of the GLSs: (a) unidirectional GLS; (b) bi-directional increasing GLS; (c) bi-directional decreasing GLS; (d) none-GLS.

the overhanging characteristics of the GLSs, the bottom surface of the GLSs and the substrate were placed at an angle of 45° during the LPBF process to avoid internal support (figure 3(c)). Process parameters used in this work were as follows: laser power of 250 W, powder layer thickness of 30 µm, scanning speed of 1200 mm s<sup>-1</sup>, and hatch spacing of 50 µm. The as-fabricated GLSs components are shown in figure 3(d).

### 2.3. Forming quality characterization and mechanical properties testing

The surface forming quality of LPBF-processed GLSs was observed by field emission scanning electron microscopy (FE-SEM, Hitachi, Japan). As shown in figure 4(a), the CMT5205 testing machine (MTS Industrial Systems, China) was used to perform uniaxial compression tests with a

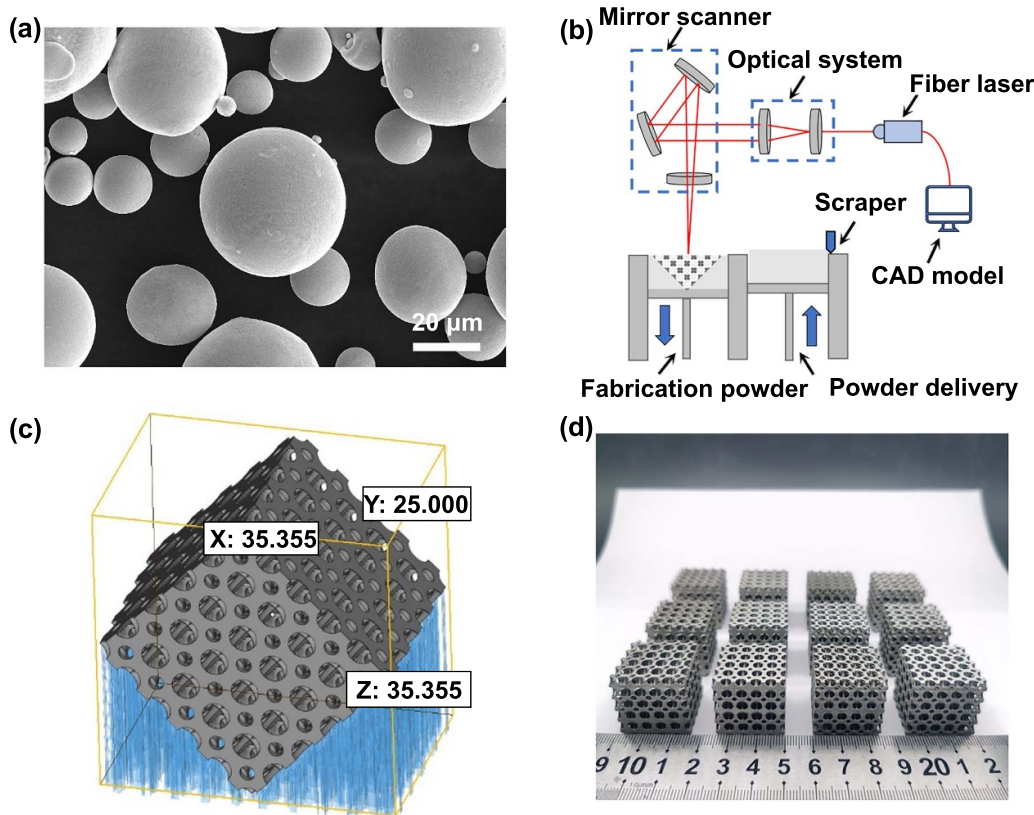


**Figure 3.** (a) The morphology of the NiTi pre-alloy powder; (b) the schematic of LPBF system; (c) relocation of the imported model; (d) as-fabricated NiTi components.

displacement rate of  $1 \text{ mm} \cdot \text{min}^{-1}$  at room temperature. The fracture morphologies after the compression tests were detected by FE-SEM.

Based on compression force–displacement curves of components, energy absorption (*EA*) and specific energy absorption (*SEA*) can be calculated. *EA* represents the energy absorbed by the structure at a specific compressive displacement. *SEA* represents the *EA* per unit mass of components. The calculation formulas are as follows:

$$\text{EA}(l) = \int_0^l F(x) dx \quad (2)$$

$$\text{SEA}(l) = \frac{\text{EA}(l)}{m} \quad (3)$$

where  $l$  represents the amount of compression displacement;  $x$  is the instantaneous displacement value;  $F(x)$  represents the applied force value;  $m$  represents the mass of components.

#### 2.4. Finite element simulation

The deformation behavior and stress distribution of the GLSs were simulated by ANSYS LS-DYNA module. The FEA model is shown in figure 4(b). The model mainly included the flexible lattice structure and the rigid plates, in which the displacement constraint was set on the bottom plate. The displacement of the top plate was set as 15 mm. The number of

nodes and elements of the model was 141 465 and 484 585, respectively. Material parameters of NiTi were obtained through standard tensile experiments. Dog-bone shape components according to the ISO 6892-1:2019 standard for tensile tests (MTS Industrial Systems, China) were fabricated alongside the lattice structures using identical process parameters. The tensile stress–strain curve of the dog-bone shape component at room temperature is shown in figure 4(c), and the obtained material parameters from figure 4(c) are shown in table 1. Referring to the previous report [52], Poisson's ratio is also listed in table 1. The elastic-plastic material constitutive model was applied in the FEA model. After the yield point, the plastic stage was defined by the data obtained from tensile stress–strain curve of the LPBF-processed NiTi sample (figure 4(c)). FEA was used to analyze the stress distribution and the compressive deformation mode of the structure. Therefore, the obtained parameters of NiTi (table 1) ignored the effects of phase transitions or twinning processes [53, 54].

#### 2.5. Phase transition analysis and shape memory effect experiments

The phase composition of NiTi samples was characterized by the x-ray diffractometer (XRD) (Bruker AXS GmbH, Karlsruhe, Germany) over a range of  $2\theta = 30^\circ$ – $90^\circ$ , and the scan rate was  $4^\circ \text{ min}^{-1}$ . The differential scanning calorimeter (DSC, METTLER TOLEDO, Switzerland) with the model of DSC 3 was used to measure the phase transition

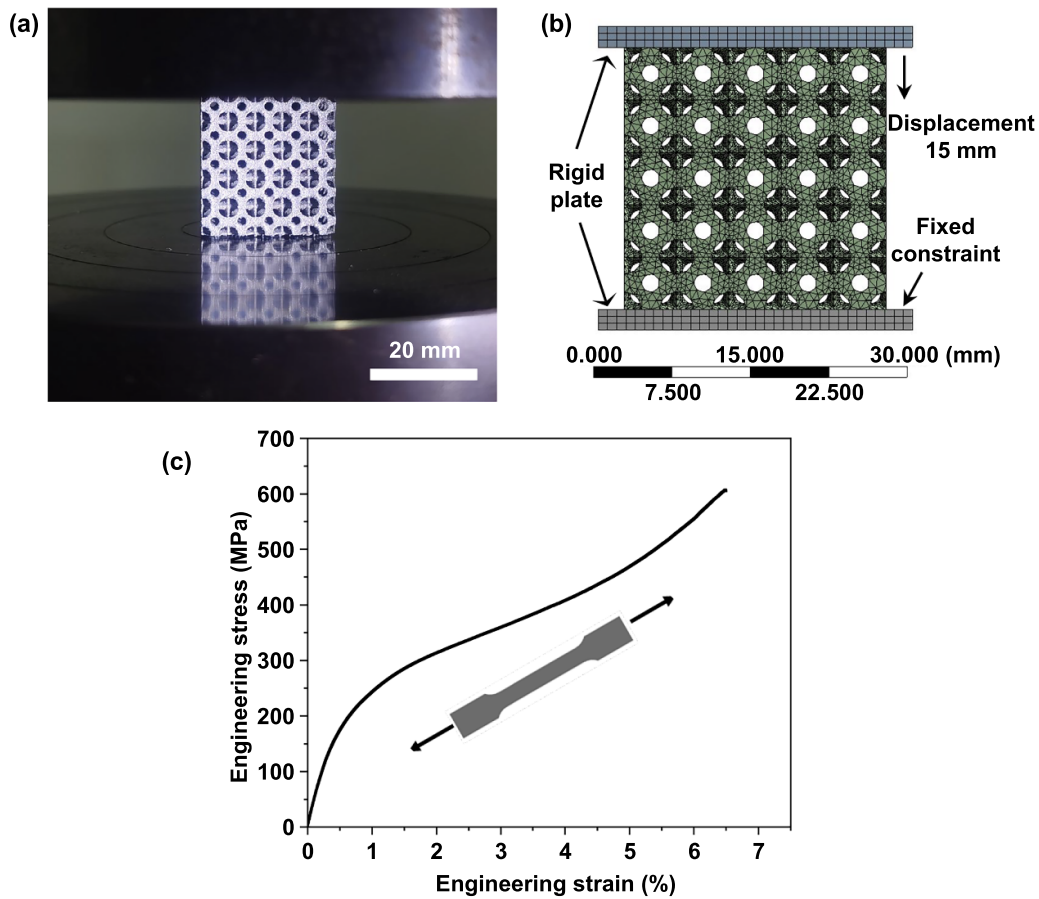


**Figure 4.** (a) Compression process image; (b) FEA model; (c) the uniaxial tensile stress–strain curve of NiTi alloy at room temperature.

**Table 1.** Material parameters of LPBF-processed NiTi components at room temperature.

Density (g·cm <sup>-3</sup> )	Young's modulus (GPa)	Poisson's ratio	Yield stress (MPa)	Ultimate stress (MPa)
6.5	43.6	0.33	228	605

temperature of NiTi alloy powders and LPBF-processed NiTi components. The DSC test temperature range was set from  $-70^{\circ}\text{C}$  to  $140^{\circ}\text{C}$  and the heating/cooling rate of the DSC tests was  $10^{\circ}\text{C min}^{-1}$ . Based on DSC curves, four transformation temperatures, at which the solid-state phase transformation occurred in NiTi, can be obtained. The start and finish temperatures of martensite and austenite transformation were defined as  $M_s$ ,  $M_f$ ,  $A_s$  and  $A_f$ , respectively.

Compression-heat cycle experiments were carried out to study the shape memory effect of NiTi components. Based on the compression force–displacement curve of components, appropriate loads were determined to carry out compression-heat cycle experiments to prevent fractures of components. In each cycle, the original height of the component was measured as  $L(n)$ . The component was loaded at room temperature ( $25^{\circ}\text{C}$ ). The displacement rate was  $1\text{ mm}\cdot\text{min}^{-1}$ . After unloading, the component was removed from the compression platform and its height was measured as  $L_1(n)$ , where  $n$  represented the number of cycles. Afterwards, the component was heated up to  $20^{\circ}\text{C}$  above  $A_f$  with a heating platform. Then the temperature was maintained for 10 min. Finally, the

component was removed from the heating platform and cooled to room temperature to eliminate the effects of thermal expansion, and its height was measured as  $L_2(n)$ . The procedure was repeated for six times.

During each cycle, the recoverable displacement rate, accumulative irrecoverable displacement, and accumulative irrecoverable strain were chosen to characterize the shape memory effect of components, which were denoted as  $\eta_{\text{rec}}$ ,  $L_{\text{irrec}}$  and  $\varepsilon_{\text{irrec}}$ , respectively. The calculation formulas are presented as follows:

$$\eta_{\text{rec}}(n) = \frac{L_2(n) - L_1(n)}{L(n) - L_1(n)} \times 100\% \quad (4)$$

$$L_{\text{irrec}}(n) = \sum_{i=1}^n (L(n) - L_2(n)) \quad (5)$$

$$\varepsilon_{\text{irrec}}(n) = \frac{L_{\text{irrec}}(n)}{L(1)}. \quad (6)$$

### 3. Results and discussion

#### 3.1. Forming quality

The surface morphologies and dimensional accuracy of LPBF-processed GLSs was shown in figure 5. The mass of the four GLSs were measured (table 2). The front of the unit cells with the relative of 0.3 (figure 5(a)) and 0.2 (figure 5(b)) are shown in the SEM images. Morphology characteristics of the hole (the white dash line) can be further observed from figure 5(c), which is the high-magnification image of the rectangular region in figure 5(a). Surface morphology of the thin wall can be further detected from figure 5(d), which is the high-magnification image of the rectangular region in figure 5(b). There were partially melted particles adhered on the component, which would increase the surface roughness of the component and reduce the forming accuracy to a certain extent. As shown in figure 5(c), the processed profile of the hole was well consistent with the designed profile, apart from some partially melted powder, indicating that the LPBF with appropriate parameters can well process round-hole structures and guarantee the processing quality. The dimensions of the unidirectional GLS, bi-directional increasing GLS, bi-directional decreasing GLS and none-GLS were measured, which were  $W$ ,  $L$ , and  $H$  respectively. Measured results are shown in figure 5(e). Since the presence of adhered powder on the  $45^\circ$  hanging surface, the length  $L$  and height  $H$  of the four components were larger than the design value, and the relative error was within 1.4% and 1.6%, respectively.  $W$  was the length between two surfaces perpendicular to the substrate, so it was the closest to the design value, and the relative error was within 0.7%.

#### 3.2. Mechanical properties and deformation process

Compressive force-displacement curves of the four GLSs are shown in figure 6(a). The compression process of four components had gone through the linear elastic stage, the fluctuate stage and the final densification stage. Combined with the tensile stress-strain curve of NiTi alloy in figure 4(c), the phase transformation behavior of the component was analyzed. Firstly, in the initial stage of deformation, elastic deformation of austenite and a small amount of martensite occurred. As the stress gradually increased, it mainly included the elastic deformation of the stress-induced martensite and the reorientation of part of the martensite. With the further increase of deformation, the reorientation of martensite increased, and the twinning and plastic deformation increased gradually until fracture, which led to a rapid decrease in structural strength. The curves showed that compression characteristics were affected by the gradient distributions. Before the densification stage, only one peak was observed in the force-displacement curves of the bi-directional increasing GLS and the none-GLS. However, for the unidirectional GLS and bi-directional decreasing GLS, multiple peaks were observed, which may be caused by layer-by-layer fracture characteristics. Figure 6(c) presents the first peak crush force of the components. The bi-directional increasing GLS exhibited the

largest first peak crush force of 34.10 kN, followed by the none-GLS (28.50 kN), unidirectional GLS (15.66 kN), and bi-directional decreasing GLS (15.25 kN). The EA and SEA of each component are illustrated in figures 6(b) and (d), respectively. Before the initial fracture, the deformation of the GLSs reached 1.89 mm (for the unidirectional GLS), 2.83 mm (for the bi-directional increasing GLS), 2.51 mm (for the bi-directional decreasing GLS), and 3.09 mm (for the none-GLS), respectively. Both the bi-directional increasing GLS and the none-GLS had higher peak fracture force and deformation at fracture, indicating that the bi-directional increasing GLS and the none-GLS would absorb more energy in the elastic stage. The EA of the bi-directional increasing GLS, bi-directional decreasing GLS and unidirectional GLS gradually exceeded that of the none-GLS, when their displacements exceeded 1.87 mm, 6.55 mm and 10.15 mm, respectively. The EA and SEA of the GLSs when displacement = 12.5 mm were shown in figure 6(d). The bi-directional increasing GLS had the highest EA (235.6 J) among four structures, followed by the bi-directional decreasing GLS (205.1 J), unidirectional GLS (175.8 J), and the none-GLS (165.6 J). The measured mass of the GLSs (listed in table 2) was used to calculate the SEA. The bi-directional increasing GLS still had the largest SEA ( $9.5 \text{ J.g}^{-1}$ ), followed by the bi-directional decreasing GLS ( $8.8 \text{ J.g}^{-1}$ ), the unidirectional GLS ( $7.2 \text{ J.g}^{-1}$ ) and the none-GLS ( $6.9 \text{ J.g}^{-1}$ ). It can be summarized that the bi-directional increasing GLS had the highest energy absorption capacity. Meanwhile, three other GLSs showed better energy absorption ability than the none-GLS.

The video frame images of the unidirectional GLS, bi-directional increasing GLS, bi-directional decreasing GLS and none-GLS during compression experiments are shown and compared in figures 7(a)-(d), respectively. Five characteristic displacement values were extracted from the compressive force-displacement curves, which were displacement = 0 mm, displacement at the first peak crush force, displacement at the end of the first peak crush force (for the unidirectional GLS, the displacement at the second peak crush force), displacement at the beginning of densification, displacement = 12.5 mm. The GLSs showed significant differences in the fracture modes. For the none-GLS, the abrupt shear fracture occurred in the component, and a shear band at  $45^\circ$  angle was formed throughout the whole component (marked by the red circle in figure 7(d)). The thin walls underwent large plastic deformation and fractured along  $45^\circ$ , which resulted in a sharp decrease in the stiffness of the none-GLS (figure 6(a)). The video frame images of the unidirectional GLS and bi-directional decreasing GLS showed that the fracture first occurred in the low-density layer. With the increase of displacements, fractures extended to layers with higher relative density, leading to the layer-by-layer fracture process (marked by the white circle in figures 7(a) and (c)). There would be a stage of force decline when each layer was fractured. As the displacement increased, the compression process of the next layer had gone through the densification and fracture stage, which in turn made the strength of the structure reach the maximum and then decrease rapidly, thus forming multiple peak values of force (figure 6(a)).

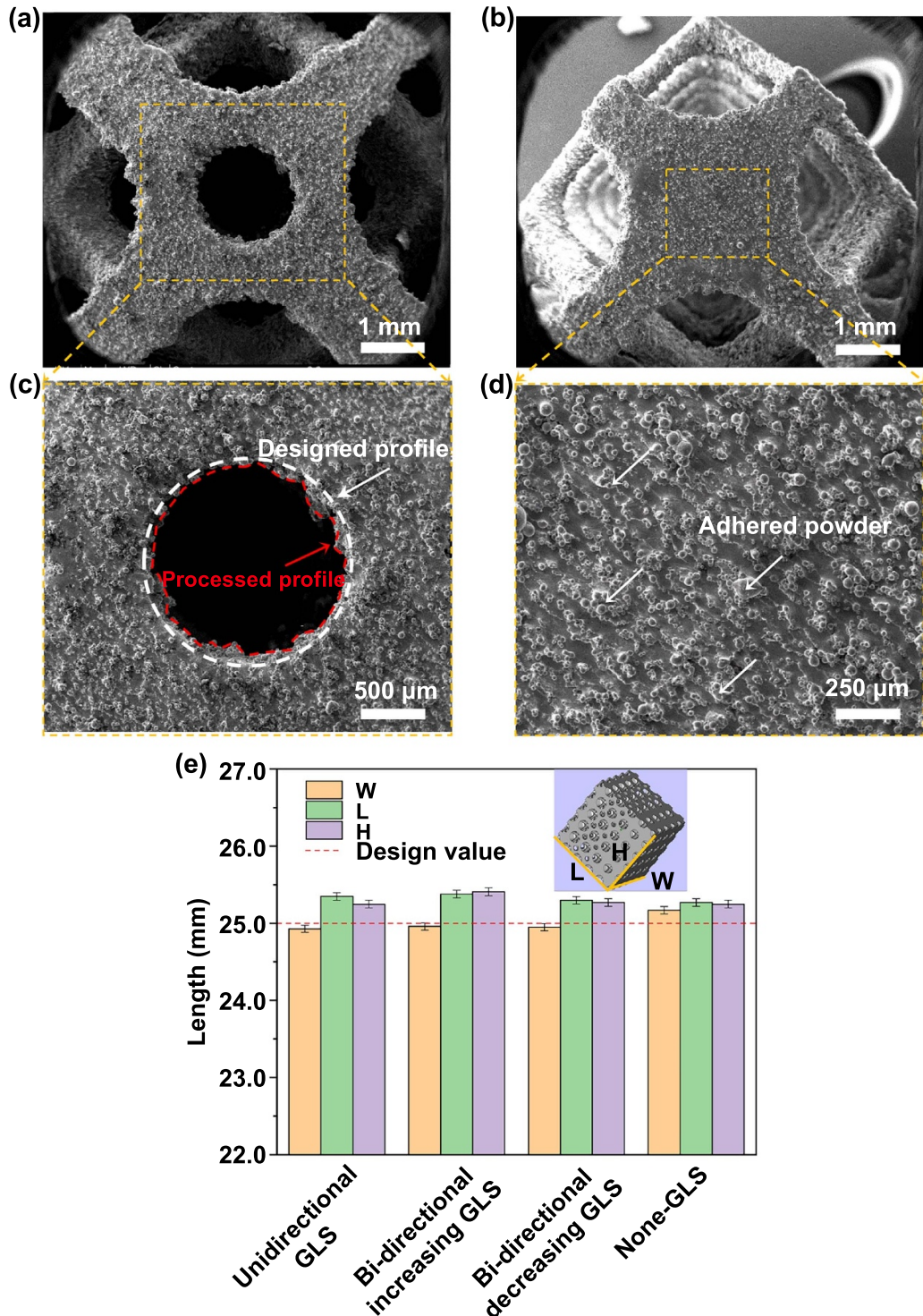


**Figure 5.** SEM micrographs and dimensional accuracy of the LPBF-processed GLSs: (a), (b) low-magnification images of the unit cell with VF of 0.3 (a) and 0.2 (b); (c), (d) high-magnification images of the unit cell with VF of 0.3 (c) and 0.2 (d); (e) dimensional accuracy of different components.

**Table 2.** The mass of LPBF-processed NiTi components.

Structure	Unidirectional GLS	Bi-directional increasing GLS	Bi-directional decreasing GLS	None-GLS
Mass	$24.55 \pm 0.02$ g	$24.69 \pm 0.01$ g	$23.37 \pm 0.01$ g	$24.00 \pm 0.01$ g

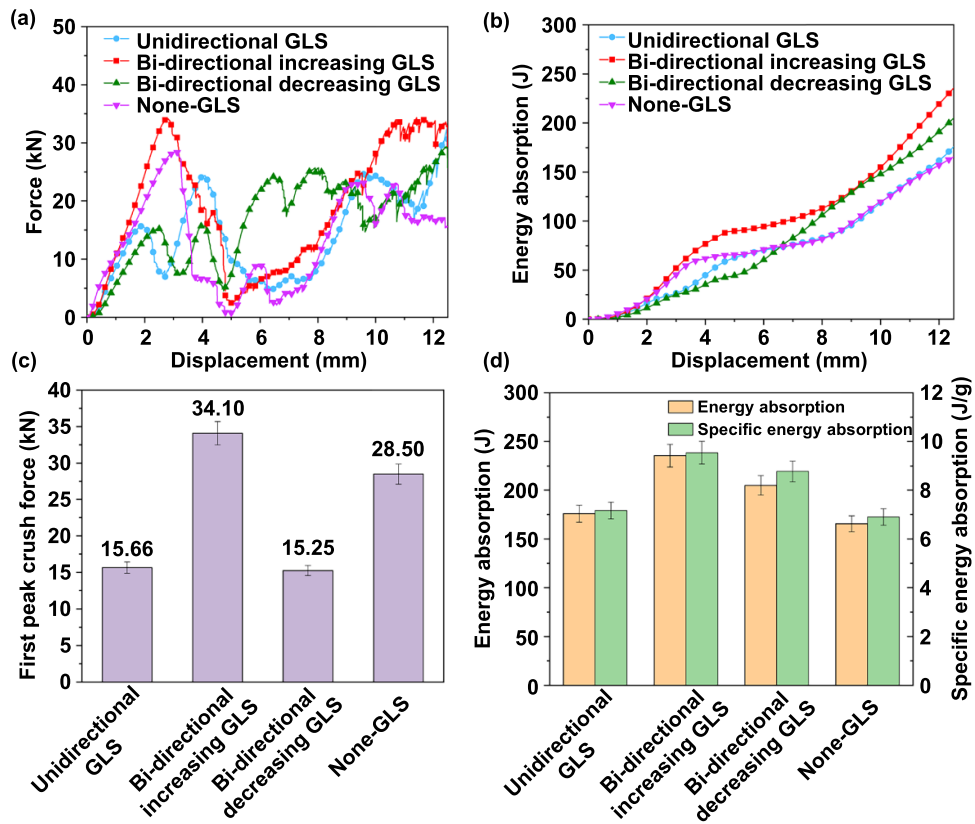


**Figure 6.** (a) Compressive force–displacement curves of four GLSs; (b) EA versus displacement curves; (c) the first peak crush force of four GLSs; (d) the EA and the SEA of four GLSs.

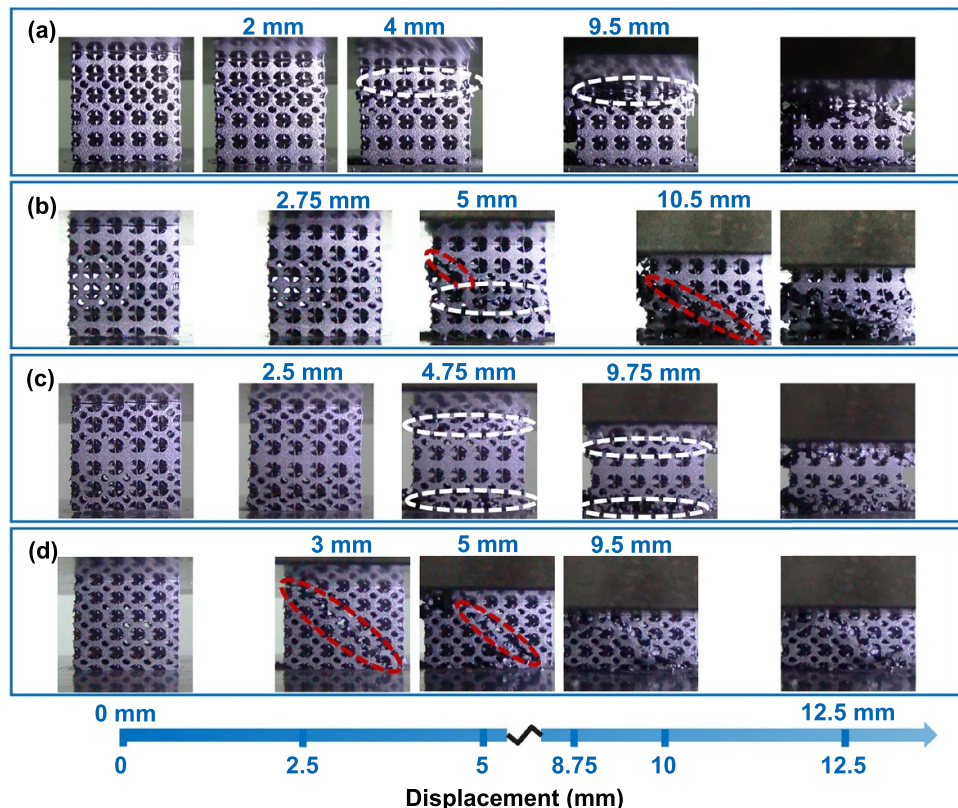


**Figure 7.** Deformation of the LPBF-processed GLSs with different gradient distributions during compression tests: (a) unidirectional GLS; (b) bi-directional increasing GLS; (c) bi-directional decreasing GLS; (d) none-GLS.

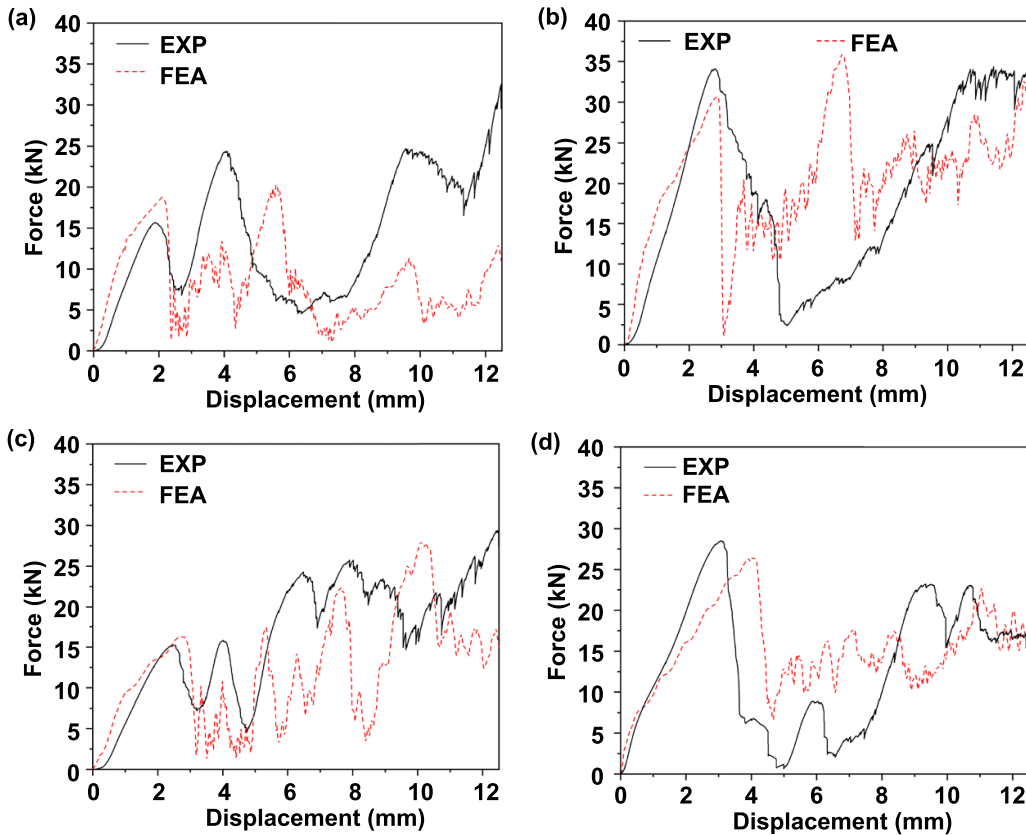


**Figure 8.** Experiment and FEA force–displacement curves of different GLSs: (a) unidirectional GLS; (b) bi-directional increasing GLS; (c) bi-directional decreasing GLS; (d) none-GLS.

As the relative densities of the different layers of the structure gradually increased, the peak compressive forces of the structure increased sequentially. Such observations have been reported previously [39, 55]. This deformation behavior was very favorable for the uni-directional impact absorption applications [37]. Interestingly, the video frame images of the bi-directional increasing GLS showed the combination of shear fracture and layer-by-layer fracture (marked by the red circle and the white circle in figure 7(b), respectively). In the early stage of deformation, layers with the lowest relative density in the bi-directional increasing GLS first fractured, showing the characteristics of layer-by-layer fracture. With the increase of displacement, fracture layers were gradually densified, and then densified fracture layers and unfractured layers with high relative density were sheared together. This unique fracture method made the bi-directional increasing GLS not only had the characteristics of higher first peak crush force but also had the characteristics of better energy absorption capacity.

The FEA of the compression deformation process of the four GLSs was conducted to research the influence of gradient distributions on stress distributions and deformation mode. The ANSYS LS-DYNA module was used in the FEA, which was shown in section 2.4. First, to verify the accuracy of the FEA model, FEA force–displacement curves of the four GLSs were compared with force–displacement curves obtained from compressive experiments. As shown in

figures 8(a)–(d), force–displacement curves of FEA and experiments had a similar trend. In force–displacement curves of FEA, the first peak crush forces of the bi-directional increasing GLS and none-GLS were greater than that of the unidirectional GLS and bi-directional decreasing GLS, which was consistent with experimental results. In addition, FEA force–displacement curves of the unidirectional GLS and bi-directional decreasing GLS also had multiple peaks crush forces, verifying the compressive behavior of the layer-by-layer fracture. Although the FEA results can better predict the actual compressive force–displacement relationship in the initial stage of structural deformation, the unconsidered phase transforming and twinning process still brought a certain deviation to the force prediction [56, 57].

Figure 9 shows Von-Mises stress distributions and deformation of the four GLSs at the displacement of the first peak crush force. For the unidirectional GLS, the stress mostly concentrated around the top of the lattice structure and the edge of the circular holes. Besides, the deformation of the unidirectional GLS mainly occurred in the second layer with low relative density (figure 9(a)). Significant plastic deformation occurred in the second layer region, the circular hole region of the unit cell changed to an elliptical shape, and the edge of the structure experienced obvious pressure-induced expansion, which was consistent with the deformation behavior observed in figure 7(a). For the bi-directional increasing GLS, the stress concentration area expanded from the middle region to both

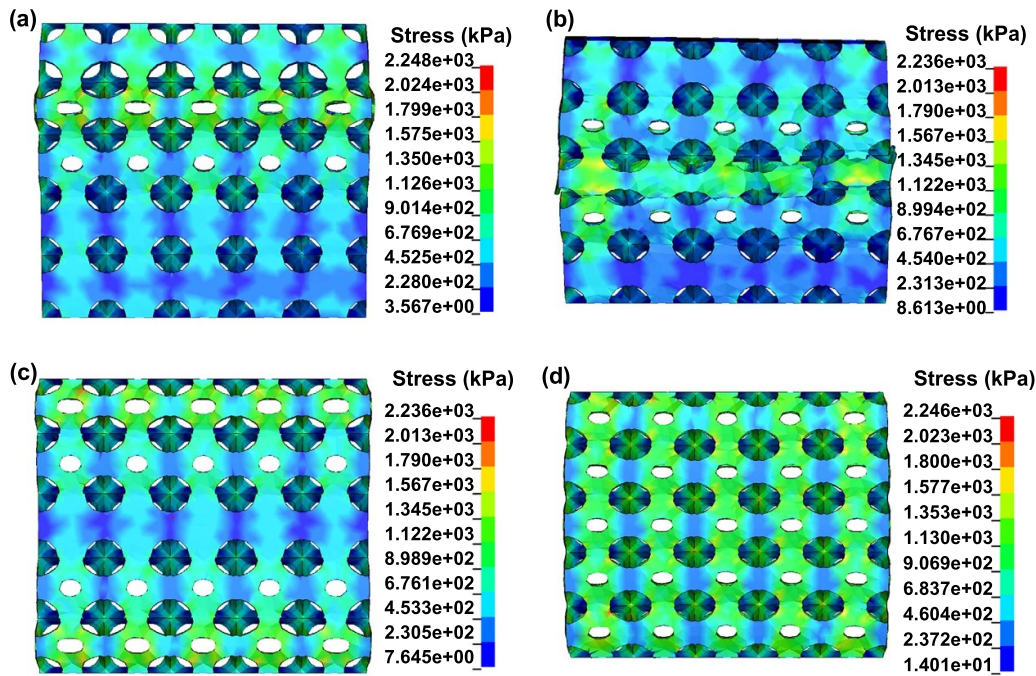


**Figure 9.** Von-Mises stress distributions and deformation of the GLSs during compression: (a) unidirectional GLS (displacement = 2.25 mm); (b) bi-directional increasing GLS (displacement = 4.35 mm); (c) bi-directional decreasing GLS (displacement = 2.55 mm); (d) none-GLS (displacement = 3.75 mm).

ends. The simulation results indicated that the deformation of the bi-directional increasing GLS mainly occurred in the middle region, such as the middle layer with the lowest relative density and the circular holes (figure 9(b)). When the middle layer with the smallest relative density began to fracture, the surrounding low-density layer also underwent large plastic deformation, and the area around the circular hole was more prone to stress concentration and cracks. The cracks between the different layers propagated each other to form an oblique fracture zone, so the structure tended to shear fracture (figure 7(b)). On contrary, for the bi-directional decreasing GLS, the stress concentration area expanded from both ends to the middle layer. The deformation of the bi-directional decreasing GLS mainly took place in the top and bottom regions (figure 9(c)). Correspondingly, during the compression of the bi-directional decreasing GLS, it was observed that the top and bottom layers were broken first (figure 7(c)). For the none-GLS, the stress concentration area and deformation had significant uniformity. The deformation started from the bending of the region near the circular holes of unit cells (figure 9(d)). The shear failure of the structure occurred when the unit cells were compacted gradually (figure 7(d)). It can be seen that the gradient distributions affected the stress distributions, thereby affecting the deformation mode of lattice structures. The low-density layer structure tended to preferentially fracture during compression, which affected the stress distribution and deformation of the surrounding area. Based on the gradient distribution design of the lattice structure, the optimization of the deformation mode and the improvement of the mechanical properties can be realized.

To further explore the fracture mode, the fracture morphology of the bi-directional increasing GLS was selected as an example (figure 10). The fracture was mainly generated in the low-density layer, as illustrated in figure 10(a). A ‘river pattern’ can be observed from figures 10(b) and (c), which was due to the crack propagation caused by stress concentration, indicating that the component had undergone brittle fracture. Further observation of the connection area of the cleavage plane, the fine dimples and typical ductile fracture feature were distributed inside the section (figure 10(d)). Fracture analysis indicated that the fracture of the bi-directional increasing GLS was a mix of ductility and brittleness, and the brittle fracture was dominant.

### 3.3. Phase transition behavior and shape memory effect

The XRD spectra of the initial NiTi powder and NiTi LPBF-processed sample are shown in figure 11(a). Three main peaks were observed in the powder and LPBF-processed sample, with orientations of (110), (002), and (211), respectively. The peak B2 phase (110) exhibited the highest intensity. NiTi precipitation phases and other impurity phases were not detected in the powder and sample. In the XRD spectra of the LPBF-processed sample, some weak peaks of monoclinic martensite (B19') were observed. XRD spectra showed that austenite and martensite exist simultaneously in the NiTi LPBF-processed sample. During the LPBF process, the evaporation and precipitation of Ni led to the uneven distribution of the elements, resulting in the microstructure with the coexistence of austenite and martensite [58].

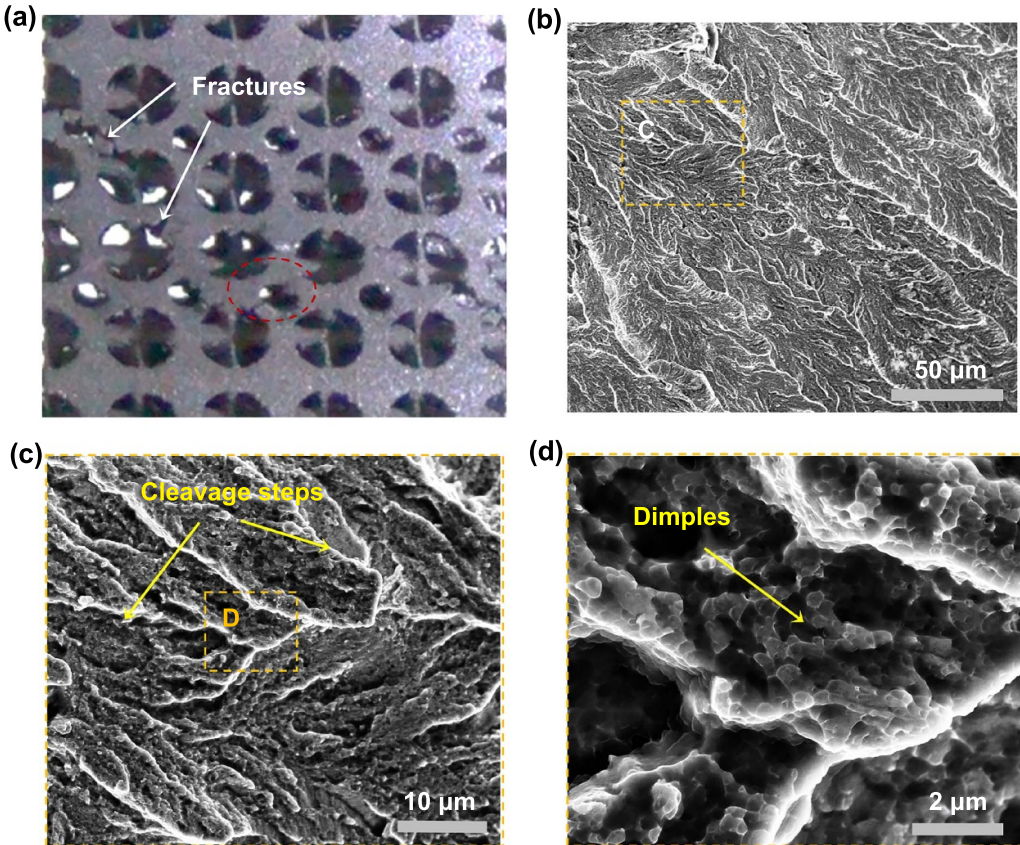


**Figure 10.** The fracture surface of the LPBF-processed bi-directional increasing GLS: (a) the image of the bi-directional increasing GLS after compression test; (b) low-magnification images (marked by red dash circle); (c) high-magnification images (region C); (d) high-magnification images (region D).

Before studying the shape memory effect of the NiTi components, the phase transition temperature of the material was measured to determine the appropriate experimental heating temperature. DSC curves of NiTi alloy powder and the sample cut from the NiTi LPBF-processed component are shown in figures 11(b) and (c). The phase transition temperatures extracted from those curves are listed in table 3. The curve of NiTi powder showed multiple peaks, which were attributed to the non-uniformity of the powder composition, indicating that the phase transition behavior of B2 (austenite)  $\leftrightarrow$  R (R phase)  $\leftrightarrow$  B19' (martensite) had occurred. This was consistent with the previous report [59] about NiTi materials. During the heating and cooling of LPBF-processed NiTi components, a reversible transformation of low-temperature martensite (monoclinic with low symmetry) to high-temperature austenite (body-centered cubic with high-symmetry) occurred, which made the NiTi components have shape memory effect under thermal stimulation. Therefore, the transformation temperature between austenite and martensite was the focus of the study of shape memory effect. The phase transition temperatures of LPBF-processed components were higher than that of the powder sample, which was related to the high-energy laser beam during the LPBF process. Ni has a lower boiling point (3186 K) than Ti (3560 K), so Ni is more likely to evaporate at higher temperatures [60]. The high energy input caused a sharp increase in temperature,

leading to the evaporation of nickel and the enrichment of titanium. The decrease of Ni content will lead to a significant increase in phase transition temperature [61]. Therefore, the  $A_f$  of the NiTi LPBF-processed sample was higher than that of NiTi powder. In the DSC curves, the phase transition peaks of the LPBF-processed NiTi sample showed an obvious broadening phenomenon. The differences in the composition, microstructures and residual stress of the molten pool of the LPBF-processed NiTi sample will lead to the difference in phase transformation temperature, thereby broadening the phase transition peaks [58].

The components with the shape memory characteristics of NiTi often bear complex cyclic loads in practical applications. Therefore, the effect of cycle numbers on the shape memory effect of NiTi components needed further study. Based on the compression force–displacement curves, the compressive peak forces for the four GLSs were 10 kN (for the unidirectional GLS), 18 kN (for the bi-directional increasing GLS), 10 kN (for the bi-directional decreasing GLS), and 18 kN (for the none-GLS), respectively. As can be seen from table 3, the  $A_f$  of the LPBF-processed NiTi components was 45.18 °C, so the heating platform was set to 90 °C in each cycle (more than 40 °C higher than  $A_f$ ). Figures 12(a)–(d) show the force–displacement curves of the four GLSs under cyclic compressive loading. In the first compression cycle, the displacement of the four GLSs was 0.624 mm (for the unidirectional GLS),

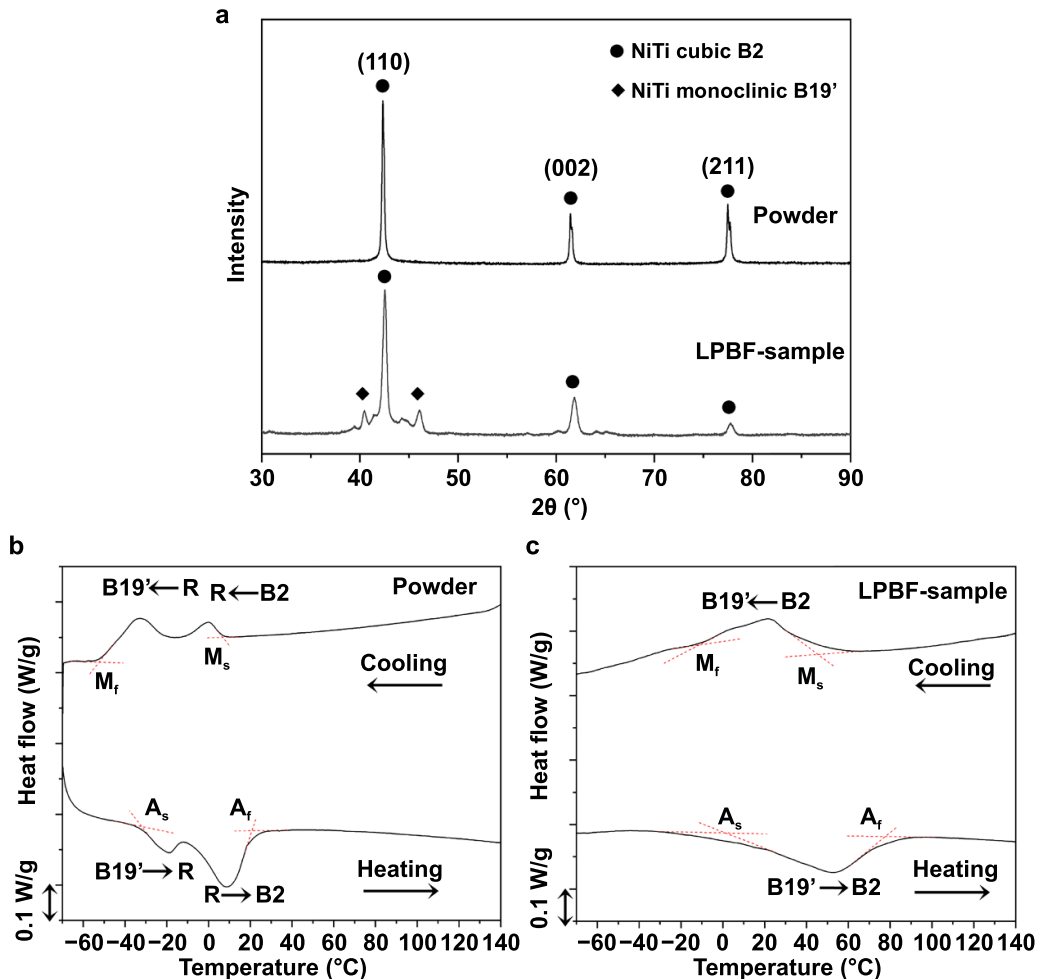


**Figure 11.** Phase transition behavior: (a) XRD spectra of the NiTi powder and NiTi LPBF-processed sample; (b) DSC curve of NiTi powder; (c) DSC curve of LPBF-processed NiTi sample.

**Table 3.** The phase transition temperatures of NiTi alloy powder and NiTi LPBF-processed sample.

	$M_f$ (°C)	$M_s$ (°C)	$A_s$ (°C)	$A_f$ (°C)
Powder	-52.43	6.85	-31.89	20.83
LPBF sample	-11.20	45.53	1.24	77.61

1.027 mm (for the bi-directional increasing GLS), 1.023 mm (for the bi-directional decreasing GLS) and 1.670 mm (for the none-GLS), respectively. The residual displacement of the four GLSs after unloading was 0.282 mm (for the unidirectional GLS), 0.528 mm (for the bi-directional increasing GLS), 0.651 mm (for the bi-directional decreasing GLS) and 1.145 mm (for the none-GLS), respectively. After heating, the recoverable displacement rate of the four GLSs reached 91.49% (for the unidirectional GLS), 89.77% (for the bi-directional increasing GLS), 89.09% (for the bi-directional decreasing GLS) and 89.52% (for the none-GLS), respectively. As shown by the red lines in figures 12(a)–(d), after six cycles, the recoverable displacement rates of the four GLSs reached 99.47% (for the unidirectional GLS), 99.15% (for the bi-directional increasing GLS), 99.58% (for the bi-directional decreasing GLS), and 99.42% (for the none-GLS), respectively. Figure 12(e) shows the recoverable displacement rate

and accumulative irrecoverable strain of the four GLSs after each cycle. The recoverable displacement rates of the GLSs increased greatly in the first three cycles, and slowed down gradually in the last three cycles, tending to 100%. The accumulative irrecoverable strain of each component in each cycle is shown in figure 12(f). With the increase of cycle number, the increase of the accumulative irrecoverable strain gradually slowed down and stabilized finally. In the first cycle, the none-GLS had the largest irrecoverable strain, followed by the bi-directional decreasing GLS, bi-directional increasing GLS and unidirectional GLS. All the GLSs had a large irrecoverable displacement. With the increase of cycle number, the orientation texture enhanced along the loading direction, which reduced the generation of irreversible twins and slowed down the growth trend of accumulative irrecoverable strain [51]. Results showed that the none-GLS had the largest accumulative irrecoverable strain. When the cycle number reached

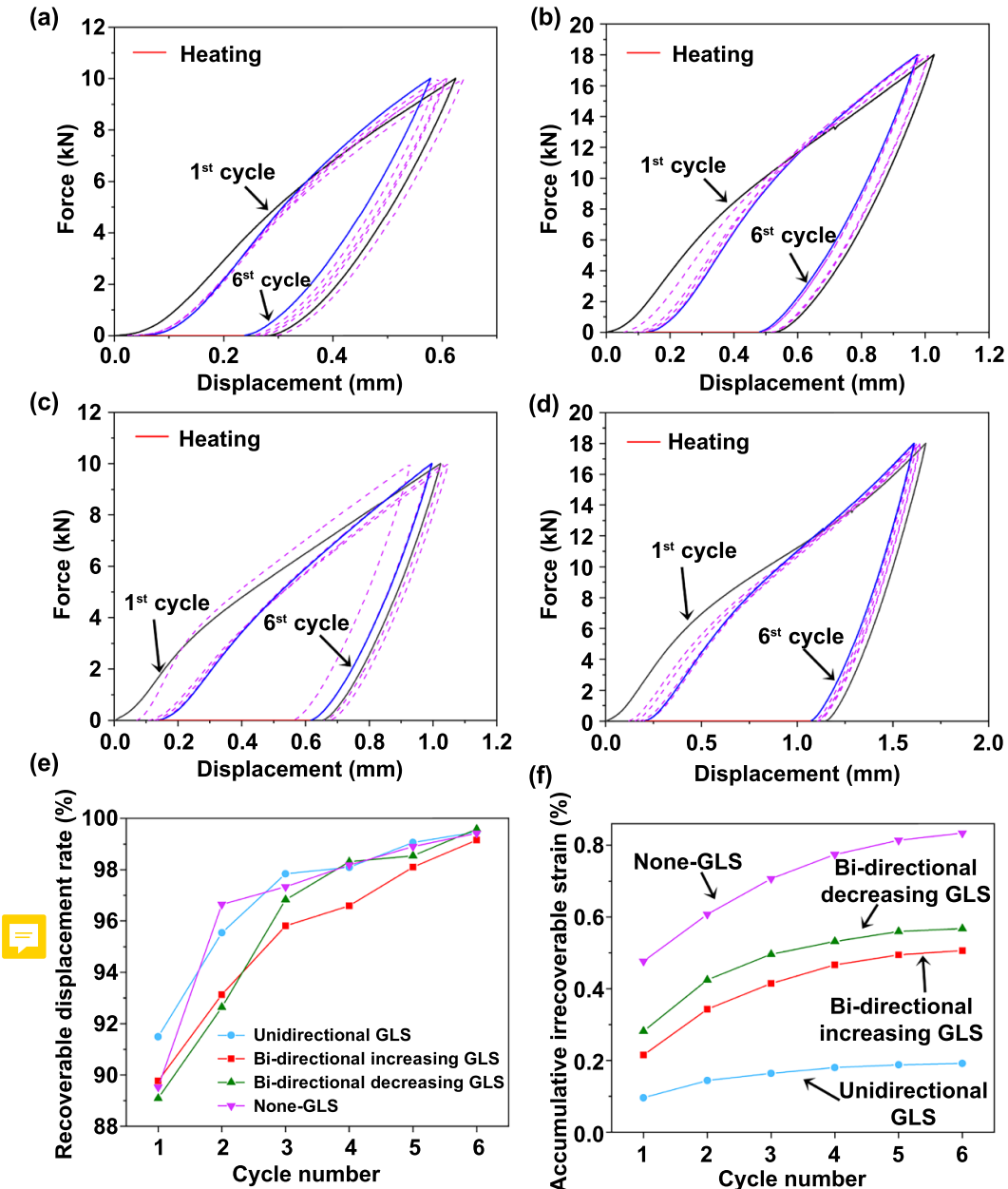


**Figure 12.** Shape memory effect of the LPBF-processed NiTi GLSs: (a)–(d) force–displacement curves of cycling tests of the unidirectional GLS, bi-directional increasing GLS, bi-directional decreasing GLS and none-GLS, respectively; (e) recoverable displacement rates of different GLSs; (f) accumulative irrecoverable strain of different GLSs.

6, the accumulative irrecoverable strain of the unidirectional GLS, bi-directional increasing GLS, bi-directional decreasing GLS and none-GLS stabilized at around 0.192%, 0.506%, 0.568% and 0.834%, respectively, indicating that the NiTi LPBF-processed GLSs had outstanding shape memory effect and functional stability.

The NiTi LPBF-processed GLSs can achieve better shape recovery within a certain displacement range. However, due to different gradient distribution designs, the displacement recovery intervals and the accumulative irrecoverable strain of the structures were different. Gradient design made the lattice structure have a larger deformation space in the compression process, so the displacement recovery intervals of the unidirectional GLS, bi-directional increasing GLS and bi-directional

decreasing GLS (figures 12(a)–(c)) were larger than that of the none-GLS (figure 12(d)). At the same time, since the none-GLS deformed uniformly as a whole during the compression process, its stress concentration and plastic deformation area were larger than those of the unidirectional GLS, bi-directional increasing GLS and bi-directional decreasing GLS, resulting in a larger accumulative irrecoverable strain (figure 12(f)).

#### 4. Conclusions

In this work, four kinds of GLSs were designed via the TO method. The unidirectional GLS, bi-directional increasing

GLS, bi-directional decreasing GLS and none-GLS were obtained by the different arrangements of the topology-optimized unit cells and then manufactured with LPBF. The energy absorption performance and shape memory effect of these components were studied. The main conclusions are as follows:

- (a) The experimental compression results showed that four kinds of GLSs had excellent compression energy absorption performance. The bi-directional increasing GLS had the highest energy absorption capacity with  $EA$  of 235.6 J and  $SEA$  of  $9.5 \text{ J.g}^{-1}$  at 0.5 strain, respectively. The unidirectional GLS, bi-directional increasing GLS and bi-directional decreasing GLS showed better energy absorption ability than none-GLS. For the unidirectional GLS and bi-directional decreasing GLS, as the relative densities of the different layers of the structure gradually increased, the peak compressive forces of the structure increased sequentially and the collapse occurred layer-by-layer. For the none-GLS, the abrupt shear fracture occurred in the component and a shear band at  $45^\circ$  angle was formed throughout the whole component. For the bi-directional increasing GLS, the collapse process was performed with the combination of the shear fracture and the layer-by-layer fracture.
- (b) The phase transformation temperatures of NiTi LPBF-processed samples were higher than that of NiTi powder due to the Ni evaporation during the LPBF process. The NiTi LPBF-processed samples at room temperature were mainly composed of austenite and a small amount of martensite.
- (c) After six cycles, the recoverable displacement rates of the four GLSs reached 99.47% (for the unidirectional GLS), 99.15% (for the bi-directional increasing GLS), 99.58% (for the bi-directional decreasing GLS), and 99.42% (for the none-GLS), respectively. The accumulative irrecoverable strains of the four GLSs started to stabilize at around 0.192% (for the unidirectional GLS), 0.506% (for the bi-directional increasing GLS), 0.568% (for the bi-directional decreasing GLS) and 0.834% (for the none-GLS), respectively. The NiTi LPBF-processed GLSs showed outstanding shape memory effect and functional stability. The gradient design made the lattice structure have a larger displacement recovery interval and a smaller accumulative irrecoverable strain.

## Acknowledgments

This work was supported by the financial support from the National Natural Science Foundation of China (Nos. 51735005 and U1930207), the Basic Strengthening Program (No. 2019-JCJQ-JJ-331), National Natural Science Foundation of China for Creative Research Groups (No. 51921003), and the 15th Batch of ‘Six Talents Peaks’ Innovative Talents Team Program (No. TD-GDZB-001).

## ORCID iD

Dongdong Gu  <https://orcid.org/0000-0002-8258-6935>

## References

- [1] Pan C, Han Y F and Lu J P 2020 Design and optimization of lattice structures: a review *Appl. Sci.* **10** 6374
- [2] Zhang C, Zhu J K, Zheng H, Li H, Liu S and Cheng G J 2020 A review on microstructures and properties of high entropy alloys manufactured by selective laser melting *Int. J. Extreme Manuf.* **2** 032003
- [3] Queheillalt D T and Wadley H N G 2005 Cellular metal lattices with hollow trusses *Acta Mater.* **53** 303–13
- [4] Ozdemir Z, Hernandez-Nava E, Tyas A, Warren J A, Fay S D, Goodall R, Todd I and Askes H 2016 Energy absorption in lattice structures in dynamics: experiments *Int. J. Impact Eng.* **89** 49–61
- [5] Cheng X M, Wei K, He R J, Pei Y M and Fang D N 2016 The equivalent thermal conductivity of lattice core sandwich structure: a predictive model *Appl. Therm. Eng.* **93** 236–43
- [6] Hu Y Y, Miles B T, Ho Y L D, Taverne M P C, Chen L F, Gersen H, Rarity J G and Faul C F J 2017 Toward direct laser writing of actively tuneable 3D photonic crystals *Adv. Opt. Mater.* **5** 1600458
- [7] Arabnejad S, Johnston R B, Pura J A, Singh B, Tanzer M and Pasini D 2016 High-strength porous biomaterials for bone replacement: a strategy to assess the interplay between cell morphology, mechanical properties, bone ingrowth and manufacturing constraints *Acta Biomater.* **30** 345–56
- [8] Gupta A and Talha M 2015 Recent development in modeling and analysis of functionally graded materials and structures *Prog. Aerosp. Sci.* **79** 1–14
- [9] Kang J F, Dong E C, Li D C, Dong S P, Zhang C and Wang L 2020 Anisotropy characteristics of microstructures for bone substitutes and porous implants with application of additive manufacturing in orthopaedic *Mater. Des.* **191** 108608
- [10] Yin S, Chen H Y, Wu Y B, Li Y B and Xu J 2018 Introducing composite lattice core sandwich structure as an alternative proposal for engine hood *Compos. Struct.* **201** 131–40
- [11] Tamburino F, Graziosi S and Bordegoni M 2018 The design process of additively manufactured mesoscale lattice structures: a review *J. Comput. Inf. Sci. Eng.* **18** 040801
- [12] Zhang L, Feih S, Daynes S, Chang S, Wang M Y, Wei J and Lu W F 2018 Energy absorption characteristics of metallic triply periodic minimal surface sheet structures under compressive loading *Addit. Manuf.* **23** 505–15
- [13] Soro N, Saintier N, Merzeau J, Veidt M and Dargusch M S 2021 Quasi-static and fatigue properties of graded Ti-6Al-4V lattices produced updates by laser powder bed fusion (LPBF) *Addit. Manuf.* **37** 101653
- [14] Gümrük R, Mines R A W and Karadeniz S 2013 Static mechanical behaviours of stainless steel micro-lattice structures under different loading conditions *Mater. Sci. Eng. A* **586** 392–406
- [15] Ushijima K, Cantwell W J, Mines R A W, Tsopanos S and Smith M 2011 An investigation into the compressive properties of stainless steel micro-lattice structures *J. Sandw. Struct. Mater.* **13** 303–29
- [16] Traxel K D, Groden C, Valladares J and Bandyopadhyay A 2021 Mechanical properties of additively manufactured variable lattice structures of Ti<sub>6</sub>Al<sub>4</sub>V *Mater. Sci. Eng. A* **809** 140925
- [17] Tancogne-Dejean T and Mohr D 2018 Stiffness and specific energy absorption of additively-manufactured metallic BCC

- metamaterials composed of tapered beams *Int. J. Mech. Sci.* **141** 101–16
- [18] Wang S, Wang J, Xu Y J, Zhang W H and Zhu J H 2020 Compressive behavior and energy absorption of polymeric lattice structures made by additive manufacturing *Front. Mech. Eng.* **15** 319–27
- [19] Du Y X, Gu D D, Xi L X, Dai D H, Gao T, Zhu J H and Ma C L 2020 Laser additive manufacturing of bio-inspired lattice structure: forming quality, microstructure and energy absorption behavior *Mater. Sci. Eng. A* **773** 138857
- [20] Lin K J, Gu D D, Hu K M, Yang J K, Wang H R, Yuan L H, Shi X Y and Meng L 2021 Laser powder bed fusion of bio-inspired honeycomb structures: effect of twist angle on compressive behaviors *Thin-Walled Struct.* **159** 107252
- [21] Meng L, Shi J X, Yang C, Gao T, Hou Y L, Song L L, Gu D D, Zhu J H, Breitkopf P and Zhang W H 2020 An emerging class of hyperbolic lattice exhibiting tunable elastic properties and impact absorption through chiral twisting *Extreme Mech. Lett.* **40** 100869
- [22] Tao W J and Leu M C 2016 Design of lattice structure for additive manufacturing *Proc. 2016 Int. Symp. on Flexible Automation* (Cleveland, OH: IEEE) pp 325–32
- [23] Wang Y 2007 Periodic surface modeling for computer aided nano design *Comput. Aided Des.* **39** 179–89
- [24] Duan S Y, Xi L, Wen W B and Fang D N 2020 Mechanical performance of topology-optimized 3D lattice materials manufactured via selective laser sintering *Compos. Struct.* **238** 111985
- [25] Gupta V and Tandon P 2015 Heterogeneous object modeling with material convolution surfaces *Comput. Aided Des.* **62** 236–47
- [26] Pasko A, Fryazinov O, Vilbrandt T, Fayolle P A and Adzhiev V 2011 Procedural function-based modelling of volumetric microstructures *Graph. Models* **73** 165–81
- [27] Nazir A, Abate K M, Kumar A and Jeng J Y 2019 A state-of-the-art review on types, design, optimization, and additive manufacturing of cellular structures *Int. J. Adv. Manuf. Technol.* **104** 3489–510
- [28] Zhu J H, Zhou H, Wang C, Zhou L, Yuan S Q and Zhang W H 2021 A review of topology optimization for additive manufacturing: status and challenges *Chin. J. Aeronaut.* **34** 91–110
- [29] Song J, Wang Y J, Zhou W Z, Fan R, Yu B, Lu Y and Li L X 2019 Topology optimization-guided lattice composites and their mechanical characterizations *Composites B* **160** 402–11
- [30] Osanov M and Guest J K 2016 Topology optimization for architected materials design *Ann. Rev. Mater. Res.* **46** 211–33
- [31] Teimouri M and Asgari M 2021 Mechanical performance of additively manufactured uniform and graded porous structures based on topology-optimized unit cells *Proc. Inst. Mech. Eng. C* **235** 1593–618
- [32] Xiao Z F, Yang Y Q, Xiao R, Bai Y C, Song C H and Wang D 2018 Evaluation of topology-optimized lattice structures manufactured via selective laser melting *Mater. Des.* **143** 27–37
- [33] Zhang L, Song B, Fu J J, Wei S S, Yang L, Yan C Z, Li H, Gao L and Shi Y S 2020 Topology-optimized lattice structures with simultaneously high stiffness and light weight fabricated by selective laser melting: design, manufacturing and characterization *J. Manuf. Process.* **56** 1166–77
- [34] Seharing A, Azman A H and Abdullah S 2020 A review on integration of lightweight gradient lattice structures in additive manufacturing parts *Adv. Mech. Eng.* **12** 1–21
- [35] Mahmoud D and Elbestawi M A 2017 Lattice structures and functionally graded materials applications in additive manufacturing of orthopedic implants: a review *J. Manuf. Mater. Process.* **1** 13
- [36] Maskery I, Hussey A, Panesar A, Aremu A, Tuck C, Ashcroft I and Hague R 2017 An investigation into reinforced and functionally graded lattice structures *J. Cell. Plast.* **53** 151–65
- [37] Choy S Y, Sun C N, Sin W J, Leong K F, Su P C, Wei J and Wang P 2021 Superior energy absorption of continuously graded microlattices by electron beam additive manufacturing *Virtual Phys. Prototyp.* **16** 14–28
- [38] Xiao L J, Song W D and Xu X 2020 Experimental study on the collapse behavior of graded Ti-6Al-4V micro-lattice structures printed by selective laser melting under high speed impact *Thin-Walled Struct.* **155** 106970
- [39] Maskery I, Aboulkhair N T, Aremu A O, Tuck C J, Ashcroft I A, Wildman R D and Hague R J M 2016 A mechanical property evaluation of graded density Al-Si10-Mg lattice structures manufactured by selective laser melting *Mater. Sci. Eng. A* **670** 264–74
- [40] Arifvianto B and Zhou J 2014 Fabrication of metallic biomedical scaffolds with the space holder method: a review *Materials* **7** 3588–622
- [41] Gu D D, Guo M, Zhang H M, Sun Y X, Wang R and Zhang L 2020 Effects of laser scanning strategies on selective laser melting of pure tungsten *Int. J. Extrem. Manuf.* **2** 025001
- [42] Wei C, Zhang Z Z, Cheng D X, Sun Z, Zhu M H and Li L 2021 An overview of laser-based multiple metallic material additive manufacturing: from macro- to micro-scales *Int. J. Extrem. Manuf.* **3** 012003
- [43] Gu D D, Shi X Y, Poprawe R, Bourell D L, Setchi R and Zhu J H 2021 Material-structure-performance integrated laser-metal additive manufacturing *Science* **372** eabg1487
- [44] Zhao D L, Liang H, Han C J, Li J J, Liu J, Zhou K, Yang C and Wei Q S 2021 3D printing of a titanium-tantalum gyroid scaffold with superb elastic admissible strain, bioactivity and *in-situ* bone regeneration capability *Addit. Manuf.* **47** 102223
- [45] Han C J, Li Y, Wang Q, Wen S F, Wei Q S, Yan C Z, Hao L, Liu J and Shi Y S 2018 Continuous functionally graded porous titanium scaffolds manufactured by selective laser melting for bone implants *J. Mech. Behav. Biomed. Mater.* **80** 119–27
- [46] Han C J, Fang Q H, Shi Y S, Tor S B, Chua C K and Zhou K 2020 Recent advances on high-entropy alloys for 3D printing *Adv. Mater.* **32** 1903855
- [47] Zhang B P, Han X S, Chen C P, Zhang W Q, Liao H L and Chen B J 2021 Effect of the strut size and tilt angle on the geometric characteristics of selective laser melting AlSi10Mg *Rapid Prototyp. J.* **27** 879–89
- [48] Wang X B et al 2020 Effect of process parameters on the phase transformation behavior and tensile properties of NiTi shape memory alloys fabricated by selective laser melting *Addit. Manuf.* **36** 101545
- [49] Elahinia M, Moghaddam N S, Andani M T, Amerinatanzi A, Bimber B A and Hamilton R F 2016 Fabrication of NiTi through additive manufacturing: a review *Prog. Mater. Sci.* **83** 630–63
- [50] Yang C X, Xu P, Xie S C and Yao S G 2020 Mechanical performances of four lattice materials guided by topology optimisation *Scr. Mater.* **178** 339–45
- [51] Ma C L, Gu D D, Gao J, Chen W, Song Y J and Setchi R 2021 Mechanical behavior of NiTi-based circular tube chiral structure manufactured by selective laser melting *Sustainable Design and Manufacturing* ed S G Scholz, R J Howlett and R Setchi (Singapore: Springer) pp 227–37
- [52] Yu C, Kang G Z, Kan Q H and Xu X 2017 Physical mechanism based crystal plasticity model of NiTi shape memory alloys addressing the thermo-mechanical cyclic degeneration of shape memory effect *Mech. Mater.* **112** 1–17

- [53] Stebner A P, Brown D W and Brinson L C 2013 Measurement of elastic constants of monoclinic nickel-titanium and validation of first principles calculations *Appl. Phys. Lett.* **102** 211908
- [54] Rajagopalan S and Little A L 2005 Elastic modulus of shape-memory NiTi from *in situ* neutron diffraction during macroscopic loading, instrumented indentation, and extensometry *Appl. Phys. Lett.* **86** 081901
- [55] Al-Saeedi D S J, Masood S H, Faizan-Ur-Rab M, Alomarah A and Ponnusamy P 2018 Mechanical properties and energy absorption capability of functionally graded F2BCC lattice fabricated by SLM *Mater. Des.* **144** 32–44
- [56] Bucsek A N, Paranjape H M and Stebner A P 2016 Myths and truths of nitinol mechanics: elasticity and tension–compression asymmetry *Shape Mem. Superelasticity* **2** 264–71
- [57] Stebner A, Gao X J, Brown D W and Brinson L C 2011 Neutron diffraction studies and multivariant simulations of shape memory alloys: empirical texture development–mechanical response relations of martensitic nickel–titanium *Acta Mater.* **59** 2841–9
- [58] Oliveira J P, Cavaleiro A J, Schell N, Stark A, Miranda R M, Ocana J L and Braz Fernandes F M 2018 Effects of laser processing on the transformation characteristics of NiTi: a contribute to additive manufacturing *Scr. Mater.* **152** 122–6
- [59] Andani M T, Saedi S, Turabi A S, Karamooz M R, Haberland C, Karaca H E and Elahinia M 2017 Mechanical and shape memory properties of porous  $Ni_{50.1}Ti_{49.9}$  alloys manufactured by selective laser melting *J. Mech. Behav. Biomed. Mater.* **68** 224–31
- [60] Wang X B, Kustov S and Van Humbeeck J 2018 A short review on the microstructure, transformation behavior and functional properties of NiTi shape memory alloys fabricated by selective laser melting *Materials* **11** 1683
- [61] Frenzel J, George E P, Dlouhy A, Somsen C, Wagner M F X and Eggeler G 2010 Influence of Ni on martensitic phase transformations in NiTi shape memory alloys *Acta Mater.* **58** 3444–58